Whole Field Measurement of Temperature in Water Using Two-Color Laser Induced Fluorescence

by

J. Sakakibara[1] and R. J. Adrian

Department of Theoretical and Applied Mechanics
University of Illinois at Urbana-Champaign
Urbana, IL 61801.

abstract

A technique is described that measures the instantaneous three-dimensional temperature distribution of water using two-color laser-induced fluorescence (LIF). Two fluorescent dyes, Rhodamine B and Rhodamine 110, are used as temperature indicators. A laser light sheet scanned across the entire measurement volume excites the fluorescent dye, and an optical system involving a color beam splitter gives the intensity distribution of the individual fluorescent dyes on two separate monochrome CCD cameras. The ratio of these fluorescence intensities at each point of the image is calibrated against the temperature to eliminate the effect of the fluctuation of illuminating light intensity. A stable thermally stratified layer was measured by this system to evaluate the total accuracy of the measurement system. The random error of the measurement was ± 1.4K with 95% confidence. Measurements of thermal convection over a heated horizontal surface show temperature isosurfaces having typical structures such as plumes, ridges and thermals.

[1]Present address: University of Tsukuba, Tsukuba 305, Japan

1 Introduction

While techniques such as particle image velocimetry are relatively well developed for the measurement of velocity fields, there are many flows in which the temperature field is of equal or even greater importance than the velocity. These flows range from thermal convection, in which buoyancy is the primary motive force, to forced convection in which heat transfer is the primary concern. In addition to being a fundamental thermo- physical variable, temperature, being a scalar, is also a simple marker that is often very useful for visualizing the structure of the flow field, especially in three dimensions. This paper describes an improved method of measuring the temperature field in water on planar domains and, by scanning, on volumetric domains, using laser induced fluorescence. Various techniques have been used previously to obtain the spatial distribution of the temperature in water. Thermo-chromic liquid crystals (TLC) are commonly used to visualize temperature qualitatively, and several researchers have reported quantitative measurements (Akino [1]; Dabiri [2], Fujisawa [3]). The color of white light scattered from the TLC particle can be calibrated against temperature and scattering angle, It is now possible to obtain quite sensitive TLC which change color from red to blue in a range of 1K or less. However, the accuracy relative to the measurement range is not large. The uncertainty found in our experiments (95% confidence) is approximately 0.1K with an available measurement range of 0.7K.

Instead of using TLC, temperature-sensitive fluorescent dyes excited by laser light can also be used as a whole-field temperature diagnostic (Nakajima [4]; Sakakibara [5] [6]; Satoh [7]). Here, the fluorescence intensity is proportional to the exciting light intensity and the concentration of the fluorescent dye. For some dyes, e.g. Rhodamine B, the fluorescence intensity depends on the temperature. This characteristic can be used to measure the temperature of the solvent if one can keep constant both the concentration and the exciting light intensity. The relative accuracy of this method is higher than that of the TLC method because it allows a wider range of variation of the temperature. Typically the accuracy is $\pm 1.5K$ over a measurement range of 40K or more. In practice, however, the exciting light intensity may vary due to several effects, including refraction of the light passing through the thermal field itself. This may cause significant error in the measurement. In order to overcome this problem, we propose a new technique which employs two fluorescent dyes whose emission intensities depend differently upon temperature.

The ratio between the two fluorescence intensities is nearly independent of the incident light intensity.

We will explain the concepts and principles in §2, and the spectral characteristics of the fluorescent dyes, including temperature dependence and the quenching effect, will be discussed in §3. After showing the transmitting and receiving optics and data acquisition system in §4, the accuracy of the method is characterized in §5, and an experimental result demonstrating the applicability of the method to natural convection over a heated horizontal surface will be shown in §6.

2 Principle

Fluorescence is a radiative decay process that occurs by electronic transitions in molecules. After a fluorescent dye molecule is exposed to an electromagnetic field, photons entering the molecule cause displacements of electrons from one region of the molecule to another. The displacement of electrons results in increased potential energy of the molecule from the ground state (S_0) to the first electronic excited state (S_1). When the energy state returns to the ground state, fluorescent light emission takes place as a radiative process. However, there are many non-radiative processes that can compete with the light emission and reduce the fluorescence efficiency. They depend on the structure of the molecule in a complicated fashion.

The ratio of the total energy emitted per quantum of energy absorbed by the molecule is called the quantum efficiency, ϕ. The fluorescence energy $I(\mathrm{Wm}^{-3})$ emitted per unit volume is defined as

$$I = I_0 C \phi \epsilon \tag{1}$$

where I_0 is the incident light flux (Wm^{-2}), C is the concentration of the dye solution ($\mathrm{m}^{-3}\mathrm{kg}$), and ϵ is an absorption coefficient ($\mathrm{m}^2\mathrm{kg}^{-1}$). In most organic dyes, the quantum efficiency ϕ is temperature dependent. The change in fluorescence intensity is normally small, usually less than a fraction of one per cent per K. However, the sensitivity of some compounds such as Rhodamine B can be as high as $2\%\mathrm{K}^{-1}$. In contrast, the absorption coefficient, ϵ, does not have significant temperature dependence, being less than 0.05here. Thus, it is possible to measure the temperature of the solution if one can keep the incident light flux, I_0, and concentration, C, constant.

As mentioned above, I_0 is affected by various agencies including convergence and divergence of the light sheet and (possibly time-dependent) refraction of the light passing through the thermal field. To avoid this problem, it is necessary to provide a means of measuring the local, instantaneous intensity of the illuminating light. This can be done using a fluorescent dye with a quantum efficiency that is not sensitive to temperature. This leads to the use of a mixture of two fluorescent dyes, called A and B whose quantum efficiencies differ. In addition, the two dyes should have different emission spectra so that the emitted light can be separated by optical means. If the two emission spectra can be perfectly separated by beam splitting optics (Fig.1), then the individual intensities can be measured by two different cameras α and β, whose voltage outputs are V^α and V^β, respectively. The ratio

$$\frac{V^\alpha}{V^\beta} = \frac{I_A}{I_B} = \frac{C_A \phi_A \epsilon_A}{C_B \phi_B \epsilon_B} \tag{2}$$

is independent of the incident light flux I_0, but it can depend on temperature through the ratio $\frac{\phi_A}{\phi_B}$. In practice, imperfect separation of I_A and I_B arises from the overlap of the emission spectrum of the two fluorescent dyes, and some fraction of I_A is detected by camera β, and some fraction of I_B is detected by camera α. In this situation, V^α and V^β can be expressed as

$$V^\alpha = F_A^\alpha I_A + F_B^\alpha I_B = I_0(F_A^\alpha C_A \phi_A \epsilon_A + F_B^\alpha C_B \phi_B \epsilon_B) \tag{3}$$

$$V^\beta = F_A^\beta I_A + F_B^\beta I_B = I_0(F_A^\beta C_A \phi_A \epsilon_A + F_B^\beta C_B \phi_B \epsilon_B) \tag{4}$$

where F_A^α and F_A^β are a fractions of the light I_A coming into the cameras α and β, respectively, and similarly for F_B^α and F_B^β. These fractions can be determined by making the concentration of one fluorescent dye zero and measuring the intensity of the light using the cameras. Let primes denote the property values extent during two experiments, one with $C_A = 0$ and the other with $C_B = 0$. For the case in which $C_B = 0$, $C_A = C'_A$, $I_0 = I'_0$, $\phi_A = \phi'_A$ and $\phi_B = \phi'_B$. Then F_A^α and F_A^β can be determined as

$$F_A^\alpha = \frac{V^\alpha_{C_B=0}}{I'_0 C'_A \phi'_A \epsilon_A}, \quad F_A^\beta = \frac{V^\beta_{C_B=0}}{I'_0 C'_A \phi'_A \epsilon_A} \tag{5}$$

Also, by making $C_A = 0$, $C_B = C'_B$, $I_0 = I'_0$, $\phi_A = \phi'_A$ and $\phi_B = \phi'_B$,

$$F_B^\alpha = \frac{V_{C_A=0}^\alpha}{I_0' C_B' \phi_B' \epsilon_B}, \quad F_B^\beta = \frac{V_{C_A=0}^\beta}{I_0' C_B' \phi_B' \epsilon_B} \tag{6}$$

Substituting (5)(6) into (3)(4), the ratio between V^α and V^β becomes,

$$\frac{V^\alpha}{V^\beta} = \frac{C_A C_B' \phi_A \phi_B' V_{C_B=0}^\alpha + C_B C_A' \phi_B \phi_A' V_{C_A=0}^\alpha}{C_A C_B' \phi_A \phi_B' V_{C_B=0}^\beta + C_B C_A' \phi_B \phi_A' V_{C_A=0}^\beta} \tag{7}$$

Here, the four values $V_{C_A=0}^\alpha$,$V_{C_B=0}^\alpha$, $V_{C_A=0}^\beta$ and $V_{C_B=0}^\beta$ are constants once the optical system is fixed. The relationship between temperature and ϕ_A, ϕ_B is dye-dependent and measurable. Therefore, the intensity ratio V^α/V^β will be a function of C_A, C_B and temperature.

By denoting the concentration ratio as $C_{A/B} = C_A/C_B$, Eq.7 can be expressed as,

$$\frac{V^\alpha}{V^\beta} = \frac{C_{A/B} C_B' \phi_A \phi_B' V_{C_B=0}^\alpha + C_A' \phi_B \phi_A' V_{C_A=0}^\alpha}{C_{A/B} C_B' \phi_A \phi_B' V_{C_B=0}^\beta + C_A' \phi_B \phi_A' V_{C_A=0}^\beta} \tag{8}$$

The concentration ratio $C_{A/B}$ could also affect the temperature sensitivity of V^α/V^β which can be evaluated by differentiating the Eq. 8 by T,

$$\frac{\partial}{\partial T}\left(\frac{V^\alpha}{V^\beta}\right) = \frac{C_A' \phi_A' C_{A/B} C_B' \phi_B' \left(V_{C_B=0}^\alpha V_{C_A=0}^\beta - V_{C_A=0}^\alpha V_{C_B=0}^\beta\right)\left(\phi_B \frac{\partial \phi_A}{\partial T} - \phi_A \frac{\partial \phi_B}{\partial T}\right)}{\left(V_{C_B=0}^\beta C_{A/B} C_B' \phi_B' \phi_A + V_{C_A=0}^\beta C_A' \phi_A' \phi_B\right)^2} \tag{9}$$

If ϕ_A and ϕ_B are comparable, good sensitivity to temperature is obtained when the temperature dependency of ϕ_A and ϕ_B differs significantly;

$$\frac{d\phi_A}{dT}\frac{d\phi_B}{dT} \quad \text{or} \quad \frac{d\phi_A}{dT} << \frac{d\phi_B}{dT} \tag{10}$$

3 Fluorescence characteristics

3.1 Selection of the fluorescent dyes

Since $d\phi/dT$ is negative for most organic fluorescent dyes, a practical method of satisfying Eq. 10 is to choose one fluorescent dye with strong temperature dependence and the other fluorescent dye with little or no temperature

dependence. Also, the emission spectra should differ enough to permit the separation of the emitted light by optical means.

Rhodamine B (RhB) has been selected as a temperature-sensitive dye for the present work, because its temperature sensitivity, 2absorption spectrum covers the range of 470-600nm, making excitation easy by conventional visible lasers, e.g. Argon-ion, Nd-YAG, etc. RhB belongs to the group of Xanthene dyes which has three benzene rings; it is commonly used as a laser dye for wavelengths near 610nm.

Candidates for the non-temperature-sensitive dye must have an absorption spectrum similar to RhB but a different emission band. Coumarine dyes, which have two benzene rings instead of three, have satisfactory spectra (λ_{abs}=455nm, λ_{em}=497nm for Coumarine 6), and they are less sensitive to temperature than RhB. However, Coumarine dyes are not soluble in water. Of the Xanthene dyes which are water soluble, Fluorescein has short wavelength absorption and emission (λ_{abs}=498nm, λ_{em}=518nm in methanol). However, Fluorescein is fairly temperature dependent ($0.6\%K^{-1}$). Another Xanthene dye Rhodamine 110 (Rh110), has similar spectral characteristics (λ_{abs}=496nm, λ_{em}=520nm), and its temperature dependence is much smaller ($0.13\%K^{-1}$). Hence we have chosen Rh110 as the non-temperature-sensitive dye.

The basic characteristics of RhB and Rh110 in water at $T = 20°C$ are summarized in Table 3.1. RhB (Aldrich, dye content > 80%) and Rh110 (Acros, laser grade) were used without further purification. Following the method described in [10] to determine the quantum efficiency, the value of ϕ for Rh110 was found by measuring the fluorescence intensity of Rh110 relative to that of RhB, as reported in [9].

Table 3.1 Basic characteristics of RhB and Rh110 (Solvent:de- ionized water, $T = 20°C$)

Dye	Molecular weight	λ_{abs} [nm]	λ_{em} [nm]	ϕ	$\epsilon_{\lambda=488}$ $[m^2g^{-1}]$	$\epsilon_{\lambda=\lambda_{RhB}}$ $[m^2g^{-1}]$	$\epsilon_{\lambda=\lambda_{Rh110}}$ $[m^2g^{-1}]$
RhB	479.02[8]	554	575	0.31[9]	4.4	1.1	5.8
Rh110	366.80[8]	496	520	0.8	34	0.073	1.1

3.2 Spectral characteristics

Figure 2 2 shows the absorption spectra of RhB (1.0mgl^{-1}) and Rh110 (1.0mgl^{-1}), and the emission spectrum of the mixture of these dyes (RhB:2.0mgl^{-1}, Rh110:0.2mgl^{-1}) measured by a spectrometer (Jobin Yvon, 270M) with a CCD camera (Sony, XC77) as a detector. The exciting light wavelength for the emission spectra measurement was λ_{ex}=488nm, and the solvent was deionized water for both absorption and emission measurements.

Emission occurs at a longer wavelength than absorption because the emissive transition occurs after some vibrational energy has been lost into surrounding molecules of the solvent [12]. The shape of the emission spectrum of the mixture of the dyes is similar to that of the simple summation of individual dye's spectra (not shown here). As expected, the emission spectrum at $T = 25°C$ has a larger value than that of $T = 29°C$ at the wavelength of maximum RhB emission (λ=575nm), and less difference at the maxima of Rh110 emission spectra (λ=520nm). Note that a shift of the emission spectrum due to the change of the temperature, such as that which occurs in quinine sulfate [10], was not observed.

The maxima of the absorption and emission spectra are almost evenly spaced approximately 30nm apart. Since the overlapping region of each absorption spectrum ranges from 480 - 530nm, the exciting light wavelength λ_{ex} should be in this range to excite both dyes at the same time. It seems appropriate to choose a wavelength at the middle of this range, e.g.λ_{ex}=514.5nm of Argon-ion laser, as the exciting light wavelength. However this wavelength almost matches the wavelength of maxima Rh110 emission, and we need to be able to separate the exciting light and emitted light by a long wave pass filter in the recieving optics, in order to eliminate the scattered light from the measurement volume. Thus, we chose the λ_{ex}=488nm line of Argon-ion laser as the exciting light wavelength in this study, instead of the 514.5nm line,.

3.3 Temperature dependence

Figure 3 shows the temperature variation of the fluorescence intensity of RhB ($5.0\times\ 10^{-2}\text{mgl}^{-1}$), I_{RhB}, and Rh110 ($2.5\ \times\ 10^{-3}\text{mgl}^{-1}$), I_{Rh110}, after being transmitted through our system of filters and splitter. The intensity is normalized by its value at $T = 20°C$. In the measurement, dye solution was contained in a glass cuvette (Spectrocell, 3.5ml,10mm path) held by

a copper cuvette holder soldered onto a copper pipe. Temperature of the dye was varied by changing the temperature of the water flowing through the copper pipe. In order to make the temperature of the dye solution in the cuvette uniform, the fluid in the cuvette was stirred by a tiny rotating glass plate. Temperature was measured by a glass-coated thermistor probe and a digital multi-meter. Fluorescence intensity was measured by the CCD camera. The temperature was increased and then decreased over a range from $15°C$ to $40°C$.

The intensity change of RhB is repeatable and significant, especially at lower temperatures. In contrast to RhB, the fluorescence intensity of Rh110 is very nearly constant. The temperature dependencies of RhB and Rh110 are, respectively, $2.3\%\mathrm{K}^{-1}$ and $0.13\%\mathrm{K}^{-1}$ at $20°C$.

According to Drexhage [11] the strong temperature dependence of RhB is attributed to the mobility of the amino groups in the dye molecule. The amino groups are rotated by the thermal energy of the solvent molecules, and rotation is enhanced with increasing temperature. In fact, one fluorescent dye, Pyronin B, which has diethyl amino groups, but no carboxylphenyl substituent, also has strong temperature dependency. If these groups do not exist, as in Rh110, or are rigidized, as in Rhodamine 101, the fluorescence quantum yield is almost independent of temperature.

The relationships between temperature and the quantum efficiency ϕ_{RhB} and ϕ_{Rh110} were obtained from values at $T = 20°C$ (see Table 3.1) as follows.

$$\phi_{RhB}(T) = \phi_{RhB}(T = 20°C)\,\frac{I_{RhB}(T)}{I_{RhB}(T = 20°C)} \tag{11}$$

$$\phi_{Rh110}(T) = \phi_{Rh110}(T = 20°C)\,\frac{I_{Rh110}(T)}{I_{Rh110}(T = 20°C)} \tag{12}$$

Note that the temperature dependence of the absorption coefficient is less than $0.05\%\mathrm{K}^{-1}$ for either fluorescent dye.

3.4 Quenching

In §3.3 the temperature dependences of the fluorescence intensity of RhB and Rh110 were discussed. Fluorescence, however, may be degraded by several other effects.

The most noticeable effect is the degradation of the fluorescence intensity caused by too much exciting light. Figure 4 shows the fluorescence intensity

of RhB (5.0×10^{-2}mgl^{-1}) and Rh110 (2.5×10^{-3}mgl^{-1}) in response to an on-off sequence of the exciting light. The dyes were contained in a planar glass cuvette ($2 \times 25 \times 45$mm^3) to prevent significant circulation of the fluid, and a laser light sheet (1/e thickness and width were 10.2mm and 0.89mm, respectively) illuminated the fluid in the cuvette. The laser light was turned on for 50 seconds, then turned off 50 seconds, and this cycle was repeated while the power of the laser was increased. The fluorescence intensity at the middle of the sheet, the brightest region, was detected by a photo-diode (BS500B, Sharp) with a filter which transmitted the wavelengths larger than 495nm. In Fig.4 the fluorescence of Rh110 decreased rapidly after the excitation started, and decayed exponentially. The effect is stronger at larger exciting light intensity. RhB also has the same tendency, but the degradation is less than that of Rh110. It is interesting that the fluorescence intensity partially recovers after turning off the light.

The decay rate at the beginning of excitation is plotted in Fig.5. With increasing laser power the decay rate increases monotonically. The degradation is caused by an increase of the population of non-fluorescent molecules which are produced by photo-chemical reactions [8]. It can be explained by a two-photon excitation process. High light flux causes an extra photon input after the transition to the upper state (S_1), and then further transition occurrs to the next state (S_n).

$$S_0 \xrightarrow{h\nu} S_1 \xrightarrow{h\nu} S_n$$

Molecules in state S_n must be considered as potentially reactive intermediates which can be deleterious.

The other effect is degradation caused by impurity of the solution. Figure 6 shows the time evolution of the fluorescence intensity of RhB in a glass cuvette (3.5ml,10mm path, Spectrocell) stirred by either a glass or a fluoropolymer-encapsulated stirring bar. The time axis starts from the time when we put the fluorescence solution and stirring bar into the glass cuvette. When the fluoropolymar stirring bar was in the solution, the fluorescence intensity dropped rapidly just after the preparation, and then recovered asymptotically. This phenomenon was not observed for the glass stirring bar. Although we tried to clean the fluoropolymer stirring bar using a detergent prior to the measurement, the results were not as good as for the glass stirring bar. Possibly, some contaminants on the fluoropolymer stirring bar dissolved in the solution and chemical reactions took place. Consequently,

we suggest using glass equipment for the actual measurement. Alternatively, the dye solution should be allowed to age for several hours after the initial preparation.

4 Measurement System and Procedure

4.1 System Configuration

The optical system consists of transmitting and receiving parts shown schematically in Fig.1. In the transmitting part, a laser beam with a wavelength of λ_{ex}=488nm emitted from an Argon-ion laser (maximum power of 488nm single line was 1.4W, Coherent, Innova70) was expanded by a cylindrical lens (f = 20mm) to form a laser light sheet in the flow field. The 1/e thickness and width of the sheet were 0.89mm and 37mm, respectively. A scanning mirror (General Scanning, 6325D) was used to sweep the light sheet in the out-of-plane direction. The scanner controller (General Scanning, CX660) was connected to a digital-to-analog convertor (National Instruments, LAB-PC) controlled by an IBM-PC compatible computer.

In the receiving optics, the fluorescent light was collected by a lens (f = 120mm, F5.6, Nikon, Nikkor-AM*ED) and split by a dichroic beam splitter (CVI, SWP-45-R570- T520-PW2025C). The distance between the lens and the object plane was approximately 650mm, and the magnification factor was 0.23. The physical size of the area of interest was 40 $\times$ 30mm^2. At 45 degree incident angle the beam splitter transmitted wavelengths $\lambda_T \leq$ 520nm and reflected the wavelengths $\lambda_R \geq$ 570nm. Between these limits the transmittance and reflectance varied continuously. The transmitted light was passed through a filter that rejected wavelengths lower than 495nm (Melles Griot, 03FCG067) to eliminate the Mie scattered light from particles in the flow. It was imaged onto CCD camera β (Sony, XC77). The reflected light was also passed through a filter that rejected wavelengths shorter than 570nm (Melles Griot, 03FCG089) to eliminate the shorter wavelengths completely. It was imaged onto CCD camera α (Sony, XC77). The positions of the emission spectrum detected by cameras and are indicated by the cross-latched regions in Fig. 7. It is clear that the CCD cameras α and β mainly detected the images of RhB and Rh110 emission, respectively.

The positions of each CCD camera were adjusted to capture the images of approximately the same area in the flow field. Since we calibrated the physi-

cal co-ordinates and the image co-ordinates (see §4.2), further positioning of the cameras was not needed. The timings of the video signals of the CCD cameras were synchronized by sending the video signal of one CCD camera to the input for the vertical synchronization of the other CCD camera. The video signals from the CCD cameras were digitized by a frame grabber (Imaging Technology, IC-PCI) with three independent A/D channels, and transferred to the host memory of the PC at 30 frames per a second. The system was able to capture up to 44 successive frames (88 interlaced fields) in 1.46s.

4.2 Calibration of Image Coordinates

To determine the correspondence between physical coordinates and image coordinates, we took images of a calibration plate which had a grid pattern with 1mm intervals printed on a light-diffusive glass plate. The surface of the plate was set in the plane of the laser light sheet and illuminated from the back by a halogen lamp. The grid image was captured by each CCD camera through the receiving optics. The location of each grid point in the image plane coordinates was automatically obtained by finding local peaks of a cross-correlation function between the grid image and a template image which had a pattern of one grid. After obtaining the correspondence between the location of each grid point in the physical coordinate and that in the image coordinate, a 3rd-order polynomial function was fitted by the least-squares method. The image coordinate (X, Y) of the physical coordinate (x, y) was expressed as a function;

$$X = \sum_{i=0}^{3} \sum_{j=0}^{3} \xi_{ij} x^i y^j \tag{13}$$

$$Y = \sum_{i=0}^{3} \sum_{j=0}^{3} \eta_{ij} x^i y^j \tag{14}$$

Here, the coefficients ξ and η were obtained by the least-square method. This procedure compensated automatically for camera mis-alignment and distortion due to refraction by the liquid interfaces. As similar procedure is discussed in detail in reference [13].

4.3 Variation of the intensity ratio against temperature

The variation of the intensity ratio V^α/V^β against temperature is shown in Fig.7 as a function of the concentration ratio. The fluorescent dye was kept in the same cuvette mentioned in §3.3, and intensity was measured using the receiving optics described in the previous sections. In the figure, symbols represent the value measured experimentally, and the curves are the values evaluated from Eq. 7. Although the theoretical curves are in reasonable agreement with the experimental values, a slight disagreement, which might have originated from error in the concentration of the dyes, could cause a significant error in the measurement if we use this theoretical curve as the intensity ratio/temperature calibration curves directly. Therefore we created the calibration curves normally the theoretical curve to match the theoretical and experimental values at a 'reference' temperature, T_{ref}. For this procedure it is required to measure the intensity ratio at T_{ref} by making a uniform temperature distribution in the flow field prior to the actual experiment.

Note that the calibration curve also depends on the location in the image, because the incident angle of the light path into the beam splitter affects the spectral characteristics of the transmitted and reflected incoming light. Therefore the intensity ratio vs. temperature calibration curves, including the four optical constants $V^\alpha_{C_A=0}$,$V^\alpha_{C_B=0}$, $V^\beta_{C_A=0}$ and $V^\beta_{C_B=0}$ in Eq. 7, should be obtained for each measurement point in the field of view.

In the Fig.7 it is obvious that the concentration ratio, C_B/C_A, affects the intensity ratio and its sensitivity to the temperature (Eq. 9). The value of V^α/V^β at $20°C$ evaluated from the Eq. 8 is shown in Fig. 8 as a solid line with symbols representing the value obtained experimentally. The value of V^α/V^β increases monotonically with increasing C_{RhB}/C_{Rh110}. An optimum value of V^α/V^β exists according to the following reasoning. If the S/N ratio of either V^α or V^β was lower than the other, measurements of V^α/V^β could not have higher S/N ratio than that of the lower one. In other words, the S/N ratio of the measurements of V^α/V^β should be maximized when the S/N ratios of both V^α and V^β are equal. Since the sensitivity of the CCD cameras were set to be equal, the S/N ratio of those cameras was the same when the V^α/V^β was unity. This condition was realized when $C_{RhB}/C_{Rh110} \simeq 20$, as shown in the Fig. 8.

Figure 9 shows the variation of the temperature sensitivity against the C_{RhB}/C_{Rh110}. It is observed that the maximum sensitivity (approximately

1.6-1.7%K^{-1}) can be realized in a range of C_{RhB}/C_{Rh110} from 20 to 40 in which the value of V^{α}/V^{β} is unity, as mentioned above. Thus, we used the concentration ratio of $C_{RhB}/C_{Rh110} = 20$ in our experiments.

5 Error estimates

To examine the random errors and bias errors, direct comparisons between the measured results and a thermister probe were made with and without perturbation of the excitation light intensity distribution. The test field was a stable, thermally stratified layer. The test apparatus was a glass container ($150 \times 150 \times 150$mm^3) with an aluminum bottom (Fig. 10). The bottom surface was uniformly cooled by cold water and the top surface was uniformly heated by an electrical heater. The container was insulated by 50mm of styrofoam. The fluorescent dye mixture was excited by a stationary laser light sheet. The dye concentrations were $C_{RhB} = 0.05$mgl^{-1} and $C_{Rh110} = 0.0025$mgl^{-1}.

The steady state vertical temperature profile was measured by a thermister probe and by LIF. To simulate fluctuations of the intensity distribution in the laser light sheet, (which would be caused by changes of the refractive index in convective conditions) the laser light intensity was perturbed by moving a scratched glass plate in the path of the illuminating laser beam.

In Fig. 11 a solid line and a dashed line show the ensemble- averaged temperature profiles measured by the LIF intensity ratio and the thermister probe respectively. The number of data at each point was 294 and the error bars represent the range of four standard deviations (95% confidence) of the data.

The reference temperature, T_{ref}, was $23.0°C$. Both profiles agree within approximately $\pm 1K$. The LIF measurement appears to be biased systematically with response to the thermister probe. Over the height of the cell the illuminating beam intensity, as indicated by V^{β}, varied from 0.006 to 0.27, a factor 46:1. The random error was $\pm$1.0K at the location where V^{β} was maximum, and it increased when the exciting light intensity decreased. The random error averaged over the whole measurement range was $\pm$ 1.4K (95% confidence), and the maximum systematic error was 1.3K. The random error was mainly caused by random noise in the CCD camera and the frame grabber.

6 Measurement of Thermal Convection from a Heated Horizontal Surface

The two-color LIF technique was used to measure the three-dimensional temperature field of thermal convection from a horizontal surface with uniform heating. The test section consisted of a rectangular box heated from below by electrical mats bonded to the lower side of a smooth 12.7mm thick brass plate, as shown in Fig. 12. The box was filled with de-ionized water with dye concentration of $C_{RhB} = 0.05\text{mgl}^{-1}$ and $C_{Rh110} = 0.0025\text{mgl}^{-1}$. Its interior horizontal dimensions were 152mm $\times$ 381mm and H=40mm depth. The top of the fluid layer was a free surface. The mean heat flux supplied by the heater was 27kWm^{-2} and the mean temperature drop from the heated surface to the center of the mixed layer was ΔT=15K. The Raleigh number was $Ra = \beta g H^3 \Delta T / \alpha\nu = 1.3 \times 10^7$, where β is the thermal coefficient of expansion, g is gravity, and α is the thermal diffusivity. To obtain a quasi-three dimensional reconstruction of the temperature field, the laser light sheet was scanned 30mm horizontally in a period of 0.73s. Images were captured every 1/60th second, so the spatial interval of successive images was 0.7mm. Figures 13(a) and 13(b) respectively show surfaces of constant temperature at time t=0.0s and 0.73s. Here the white grids represent the horizontal surface and the intervals are 1mm each. The laser light sheet was parallel to the y-axis and swept in the direction of the x- axis. The flow field was dominated by turbulent structures having the forms of plumes and ridges. The plumes, which consist of columns of buoyant fluid rising up from the thermal boundary layer, connected to the ridges lying on the surface. These ridges originate from instabilities of the thermal boundary layer at the intersection of the cell, or nodes of the ridges.

Figure 14 shows the temperature distribution on a horizontal (x-y) plane in the vicinity of the surface. This figure demonstrates the ability of the present technique to reconstruct x-y data from successive x-z data, albeit subject to small errors associated with evolution of the field during the scan time and refraction by turbulent temperature gradients. The temperatures at the nodes are much higher than in other parts of the ridges, or inside the cells. As the fluid inside a cell convects toward the ridges, the accumulation of the heat at the node makes the boundary layer thicker and creates more buoyancy at the node where the plumes rise upwards.

7 Conclusion

A new technique for the whole-field, non-intrusive measurement of water temperature has been described and demonstrated. It uses two fluorescent dyes, one to sense temperature and the other to sense the intensity of illumination. Rhodamine B was used for the temperature-sensitive indicator, and Rhodamine 110 was used for the non- temperature-sensitive indicator. The principal measured quantity is the ratio of the intensity of the light emitted by the Rhodamine B divided by the intensity of the light emitted by Rhodamine 110. This ratio is independent of variation of the illuminating beam intensity. Measurements of a stable stratified layer shows that the random error was ± 1.4K (95% confidence) and the maximum bias error was 1.3K. The technique is simple enough to permit reconstruction of three-dimensional temperature fields by scanning the light sheet. Applications of the current technique to the thermal convection over the heated horizontal surface shows typical structures in the form of plumes and ridges.

The present technique can be improved if a fluorescent dye having greater sensitivity can be found. The accuracy can also be enhanced by using cameras having 10- or 12-bit resolution with correspondingly less noise. The ideal pair of fluorescent dyes for these technique would have similar absorption spectra and non-overlapping emission spectra.

8 Acknowledgments

This research was supported by NSF Grant ATM 95-2266. JS held a Research Fellowship of the Japan Society for the Promotion of Science for Young Scientists (No.4941). We also wish to acknowledge Prof.M.Maeda and Prof.K.Hishida in Keio University for their collaboration.

References

[1] Akino, N.; Kunugi, T.; Ueda, M.; Kurosawa, A. 1988 Liquid-crystal thermometry based on automatic color evaluation and applications to measure turbulent heat transfer. Transport phenomena in turbulent flows theory, experiment, and numerical simulation, (Ed. Hirata, M.; Kasagi, N.) 807-820. Hemisphere

[2] Dabiri, D., Gharib,M., 1991: Digital particle image thermometry: the method and implementation. Exp. Fluids 11, 77-86

[3] Fujisawa, N.; Adrian, R.J.; Keane, R.D. 1997: Three-dimensional temperature measurement in turbulent thermal convection over smooth and rough surfaces by scanning liquid crystal thermometry. Proc. of Int. Conf. on Fluid Engineering, JSME centennial grand congress, Tokyo 1037-1042

[4] Nakajima, T.; Utsunomiya, M.; Ikeda, Y.; Matsumoto, R. 1990: Simultaneous measurement of velocity and temperature of water using LDV and fluorescence technique. 5th Int. Symp. on Appl. of Laser Tech. to Fluid Mech. Lisbon, 2.6.1-2.6.6

[5] Sakakibara,J.; Hishida,K.; Maeda,M. 1993: Measurements of thermally stratified pipe flow using image-processing techinques. Exp. Fluids 16, 82-96

[6] Sakakibara,J.; Hishida,K.; Maeda,M. 1997: Vortex structure and heat transfer in the stagnation region of an impinging plane jet (simultaneous measurement of velocity and temperature fields by DPIV and LIF). Int. J. Heat Mass Transfer 40, 13, 3163-3176

[7] Satoh, K.; Kasagi, N. 1997: Combined velocity and scalar field measurement with the simultaneous use of scanning PIV and LIF. The 10th International Symposium on Transport Phenomena in Thermal Science and Process Engineering(ISTP10) to be published.

[8] Jones, G. II, 1990: Photochemistry of laser dyes. Dye Laser Principles with applications (Ed. Duarte F.J.; Hillman, L.W.) 287-343. Academic Press

[9] Arbeloa, T.L.; Estevez, M.J.T.; Arbeloa, F.L.; Aguirresacona, I.U.; Arbeloa, I.L. 1991: Luminescence properties of rhodamines in water/ethanol mixtures. J. Luminescence 48 & 49: 400-404

[10] Guilbault, G.G. 1973: Practical Fluorescence:Theory, Methods, and Techniques. Marcel Dekker

[11] Drexhage, K.H. 1977: Structure and properties of laser dyes. in Dye Lasers (Ed. Schäfer,F.P.) 144-193. Springer

[12] Atkins, P.W. 1994: Physical Chemistry. Freeman

[13] Solof, S.; Adrian, R.J.; Liu, Z. 1997: Distortion compensation for generalized stereoscopic particle image velocimetry. Meas. Sci Tech. : .

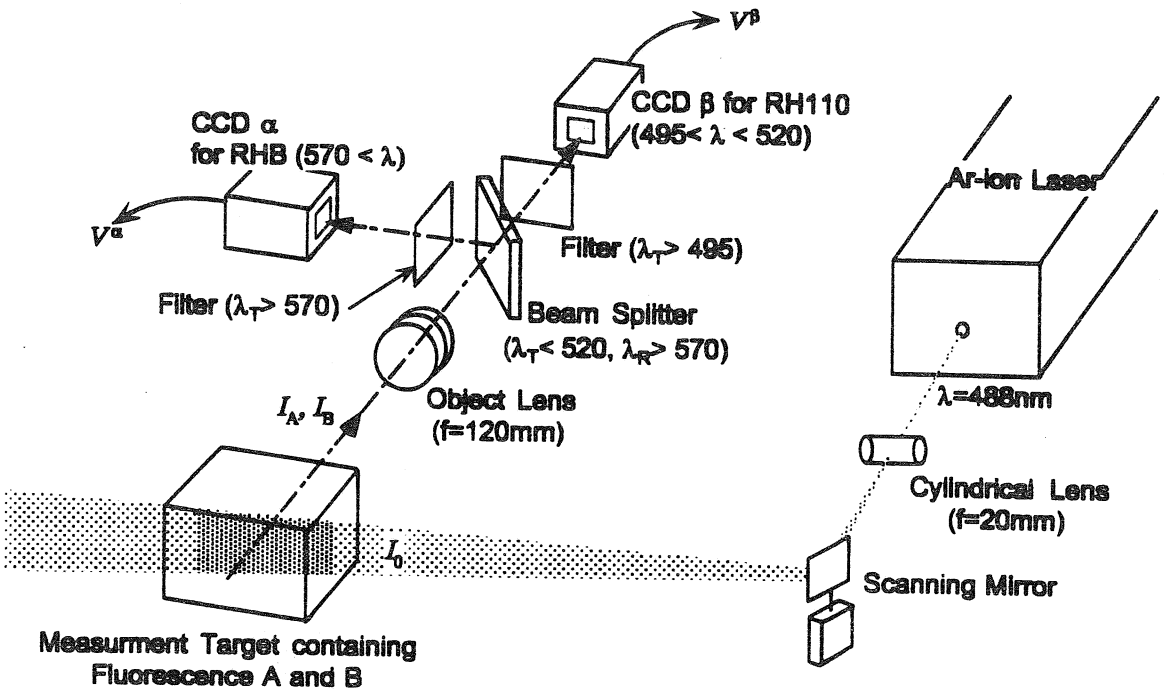

Figure 1. Arrangement of the optical components.

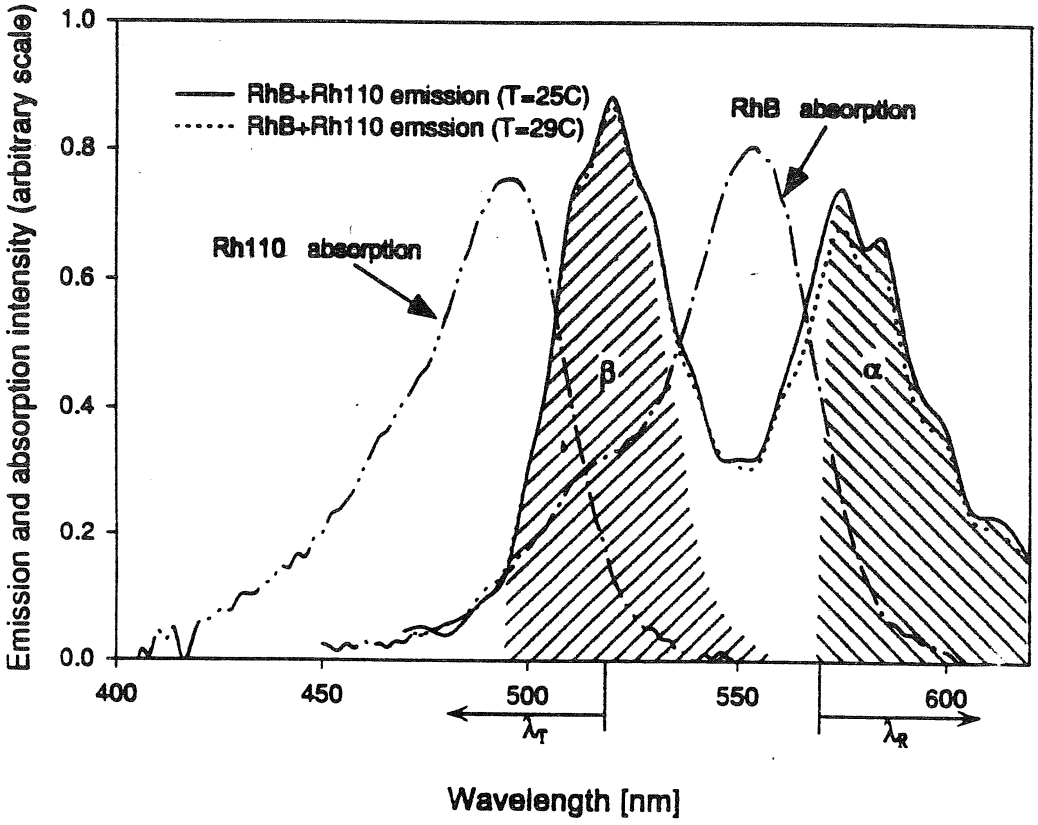

Figure 2. Emission and absorption spectra of a mixture of RhB and Rh110 (C_{RhB} = 2.0 mg/l, C_{Rh110} = 0.2 mg/l).

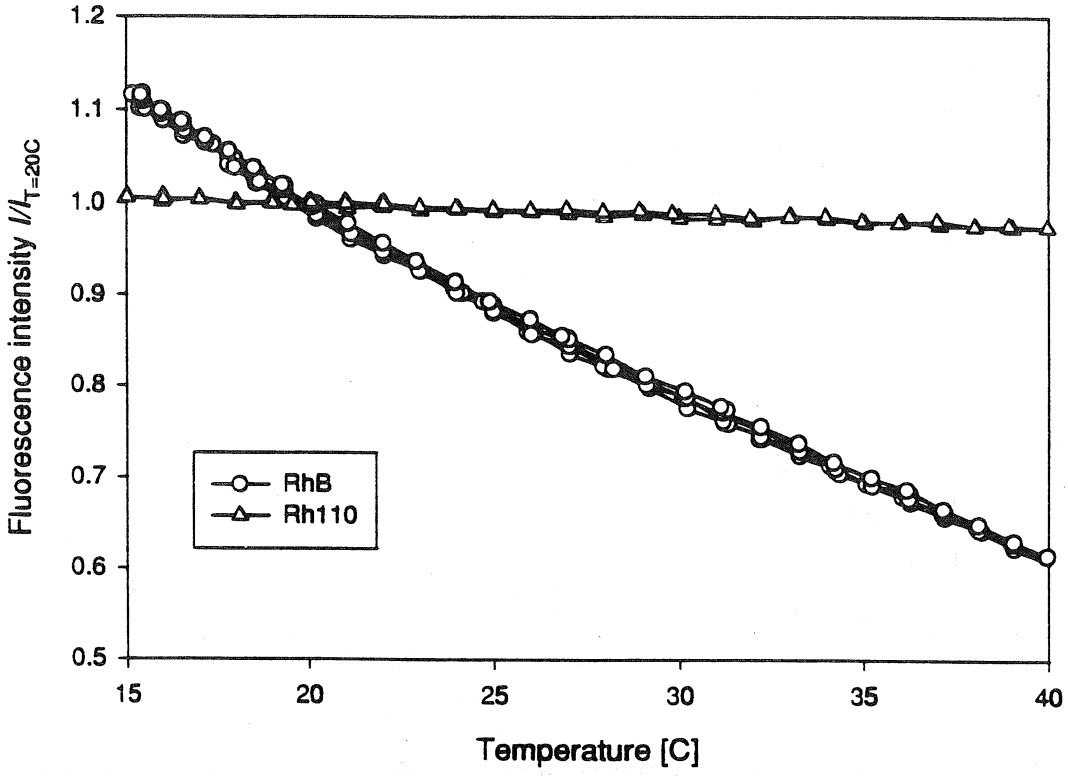

Figure 3. Variation of the fluorescence intensity against temperature.

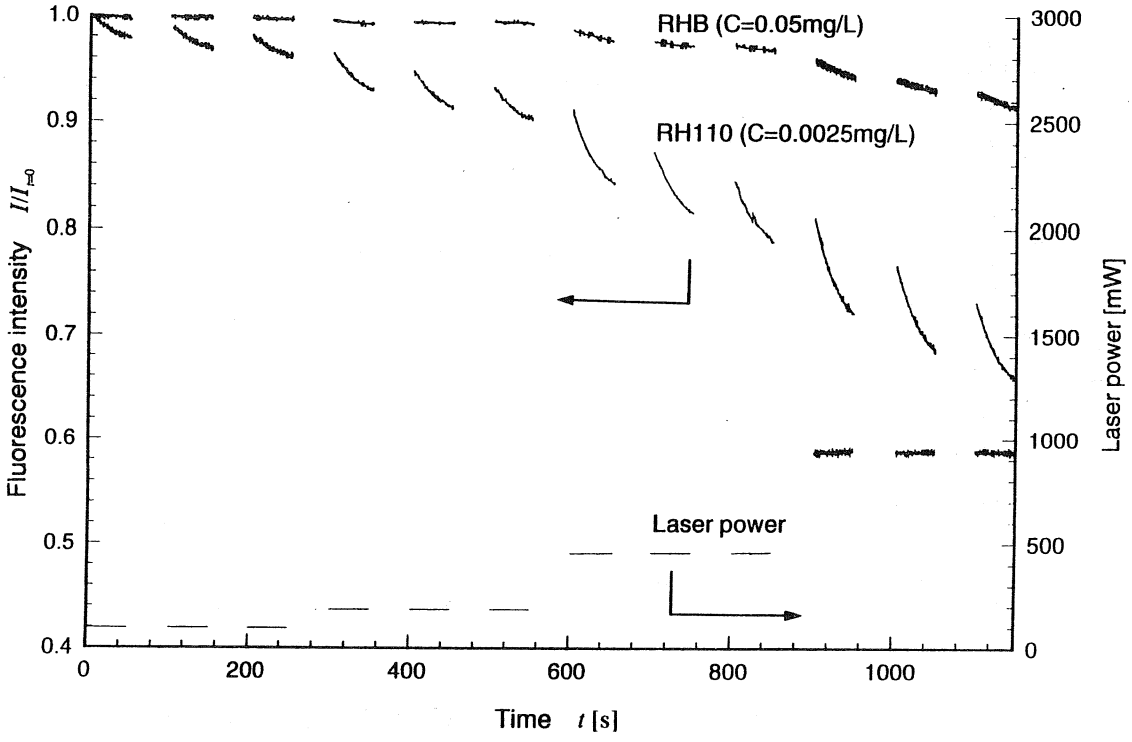

Figure 4. Time evolution of the fluorescence intensity of RhB (5×10^{-2} mg/l) and Rh110 (2.5×10^{-3} mg/l) with intermittent excitation.

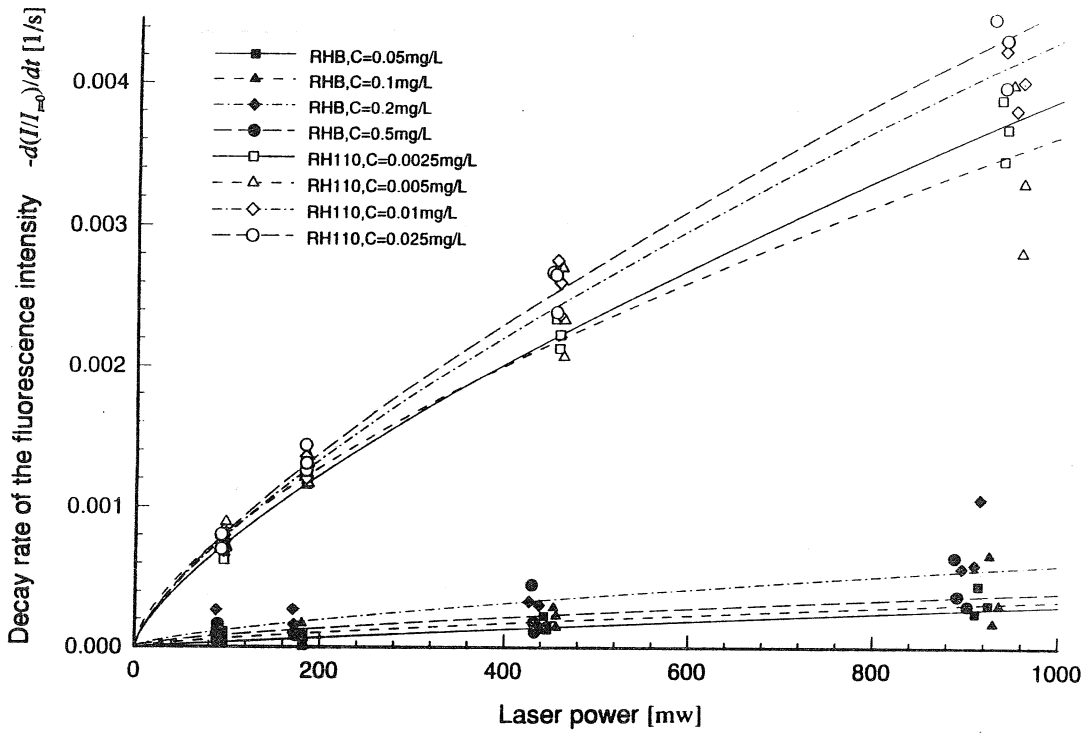

Figure 5. Decay rate of the fluorescence intensity at the beginning of the excitation.

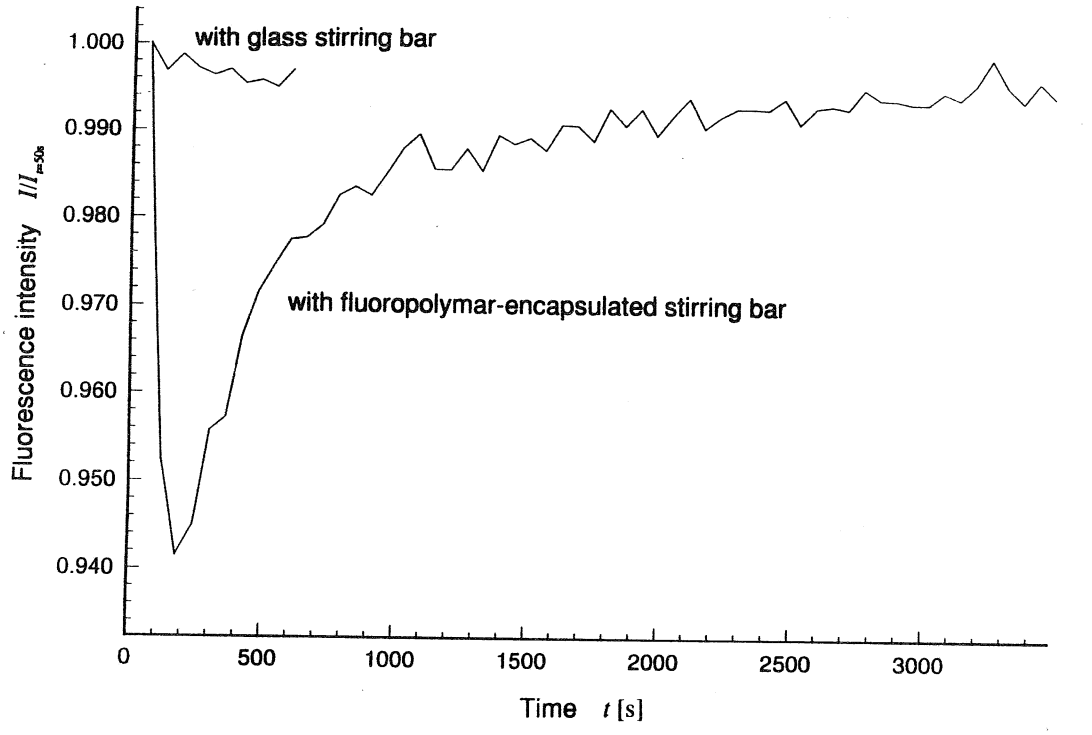

Figure 6. Time evolution of the fluorescence intensity of RhB with glass or fluoropolymer-encapsulated stirring bar.

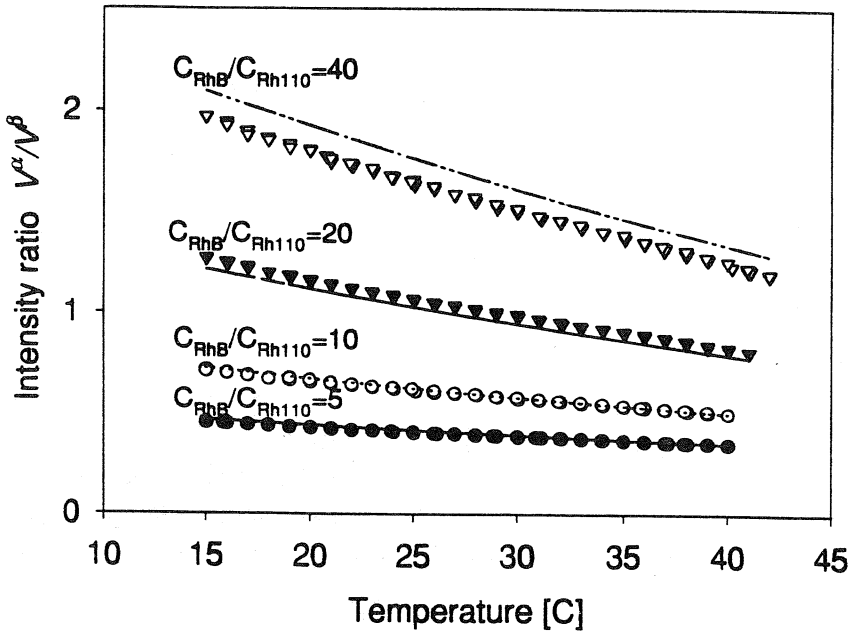

Figure 7. Variation of the ratio between two CCD cameras' output against temperature.

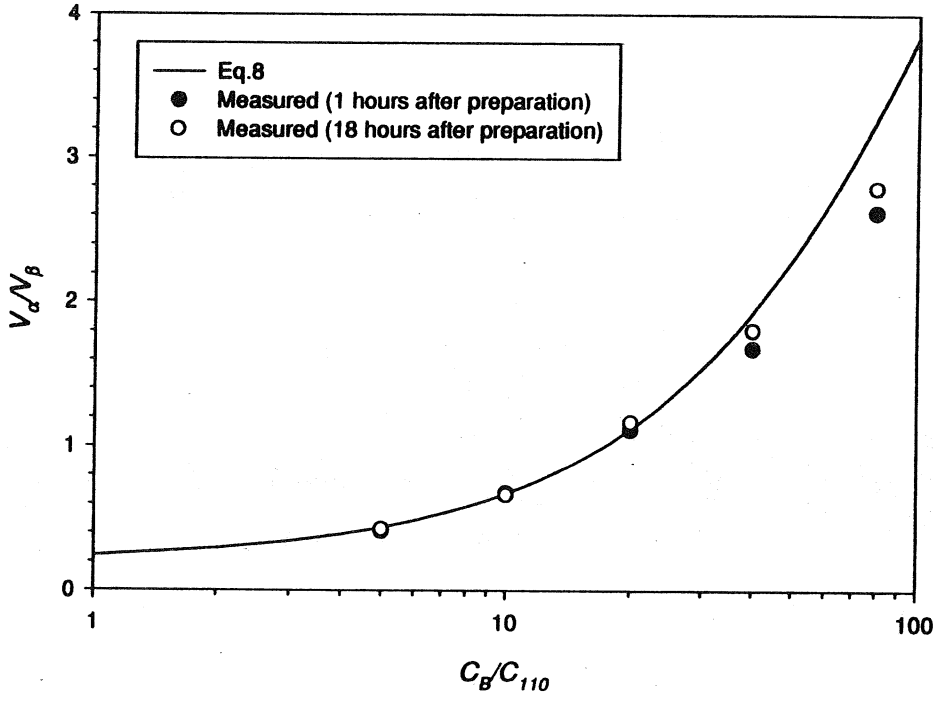

Figure 8. Variation of the ratio between two CCD cameras' output against the concentration ratio C_{Rh110}/C_{RhB}.

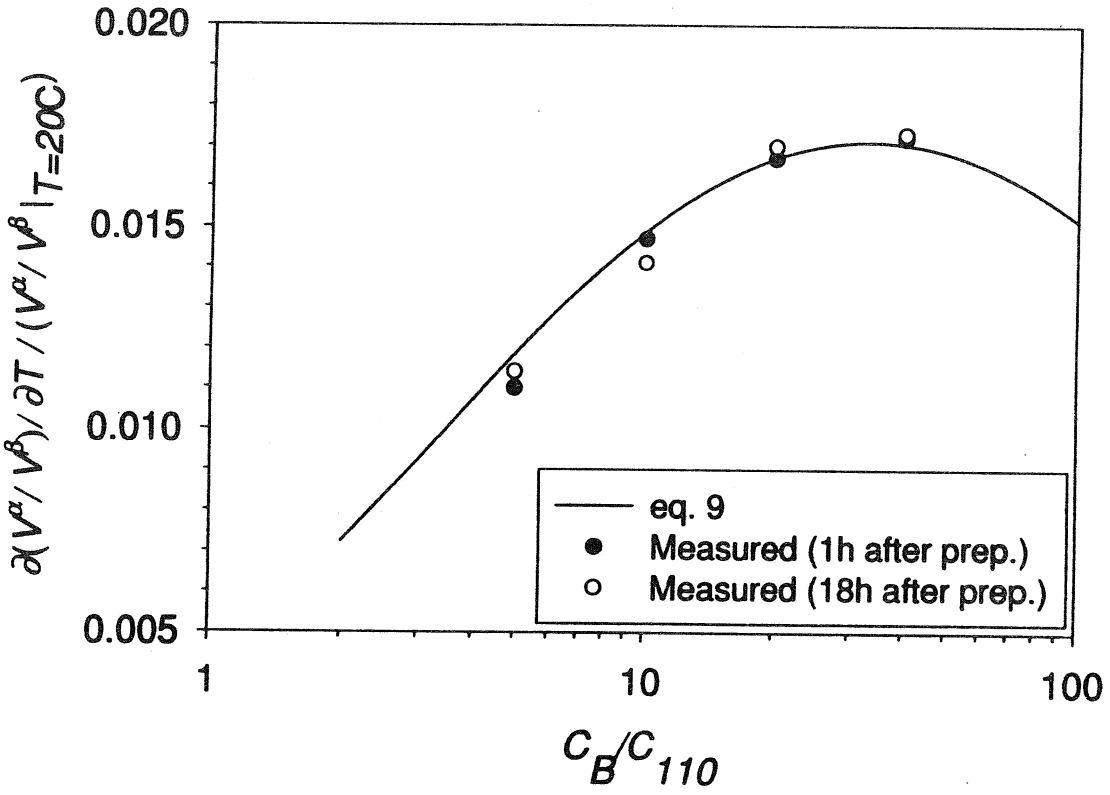

Figure 9. Variation of the temperature sensitivity of ratio of the CCD cameras' outputs against the concentration ratio C_{Rh110}/C_{RhB}.

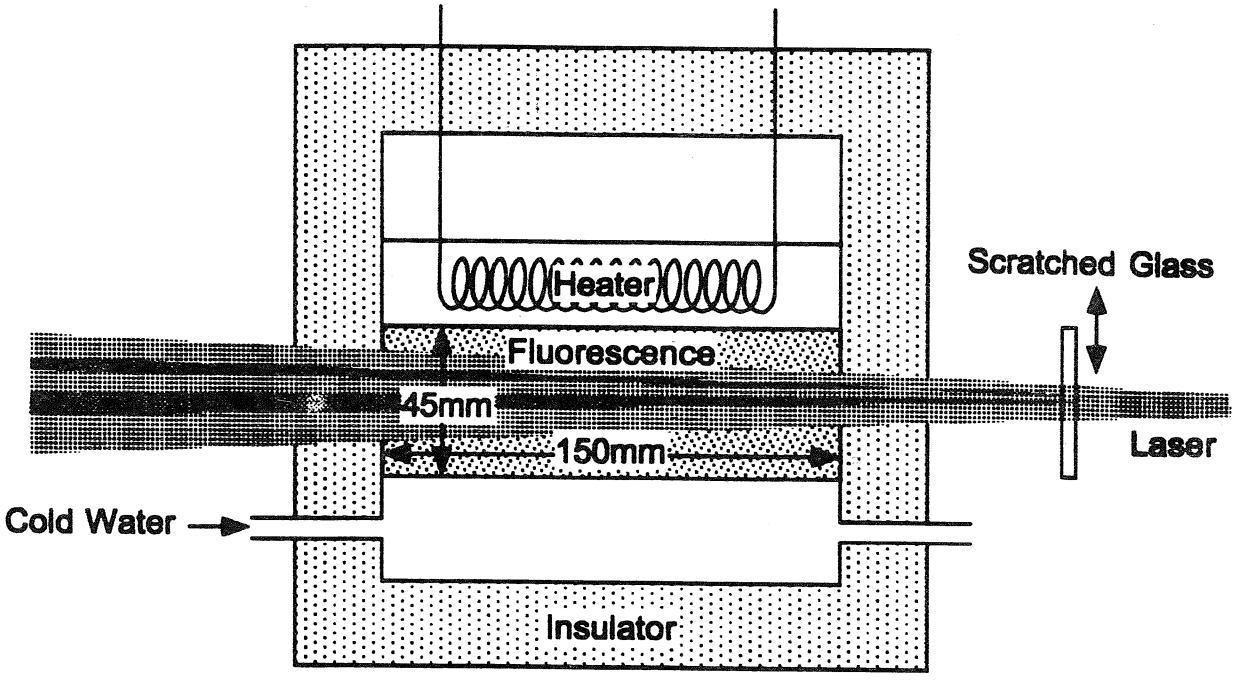

Figure 10. Experimental apparatus for the stable thermally stratified layer.

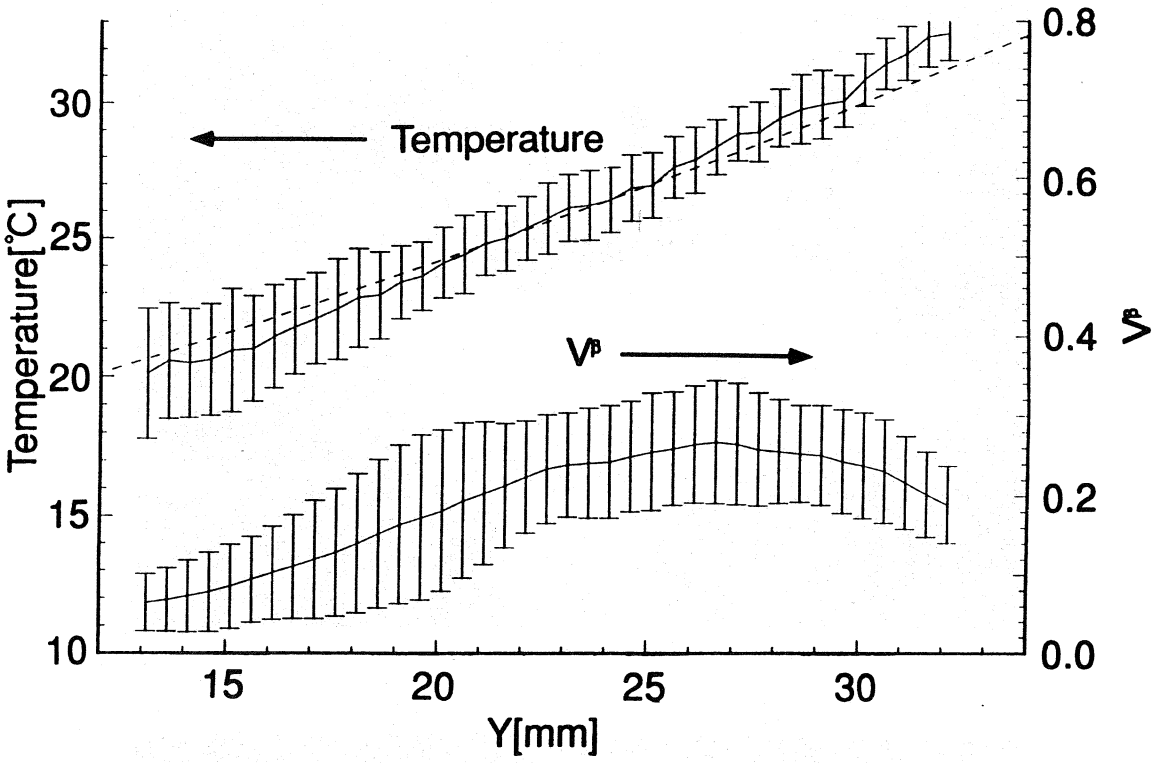

Figure 11. Temperature profile of the stable thermally stratified layer. Laser light intensity is proportional to V^β.

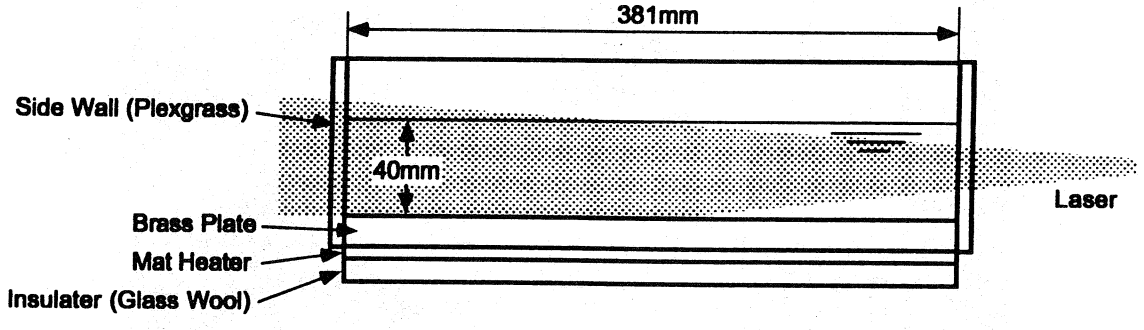

Figure 12. Experimental apparatus for natural convection over a heated horizontal surface.

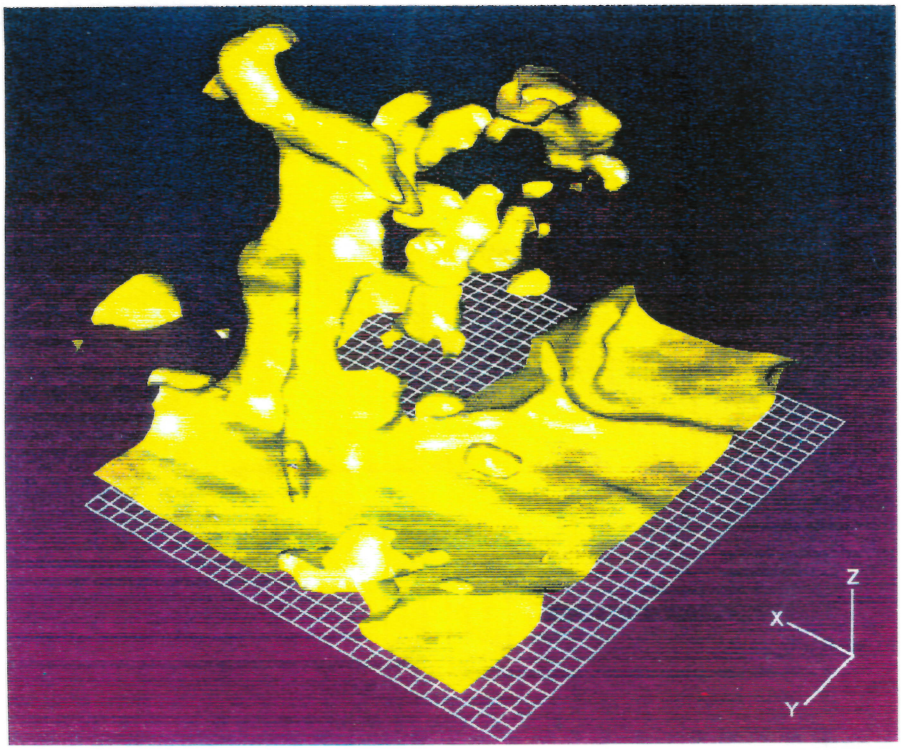

(a) $t = 0$ s

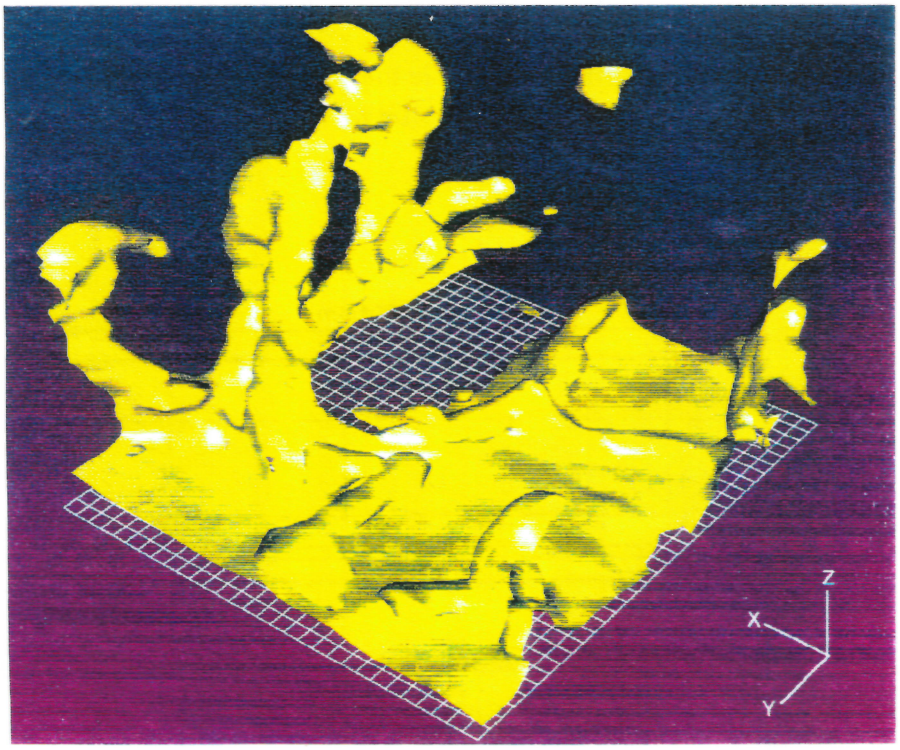

(b) $t = 0.73$ s

Figure 13. Surfaces of constant temperature of natural convection over a horizontal heated surface.

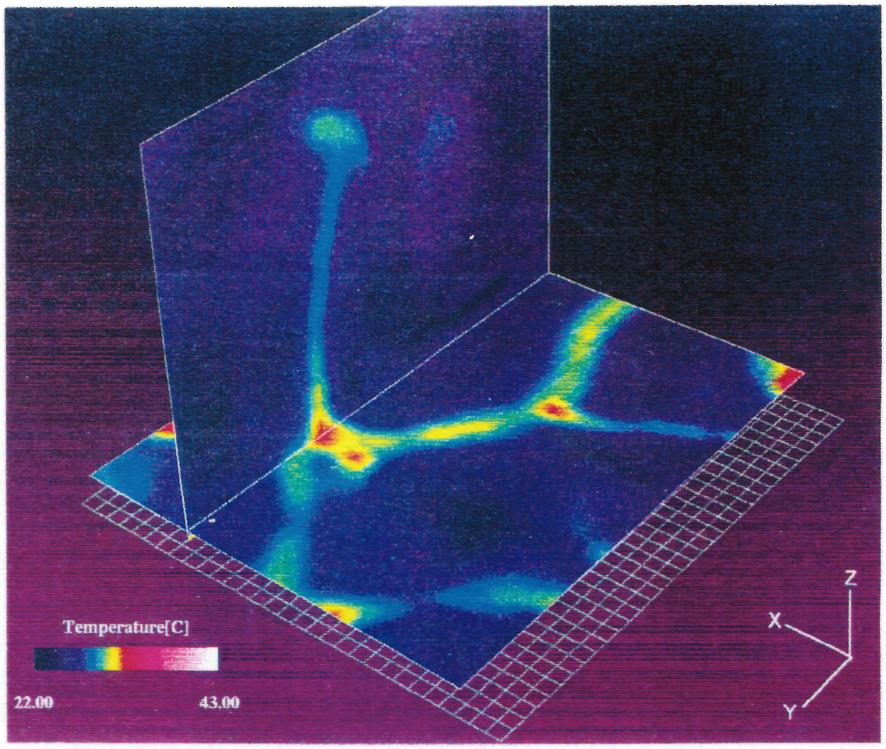

(a) $t = 0$ s

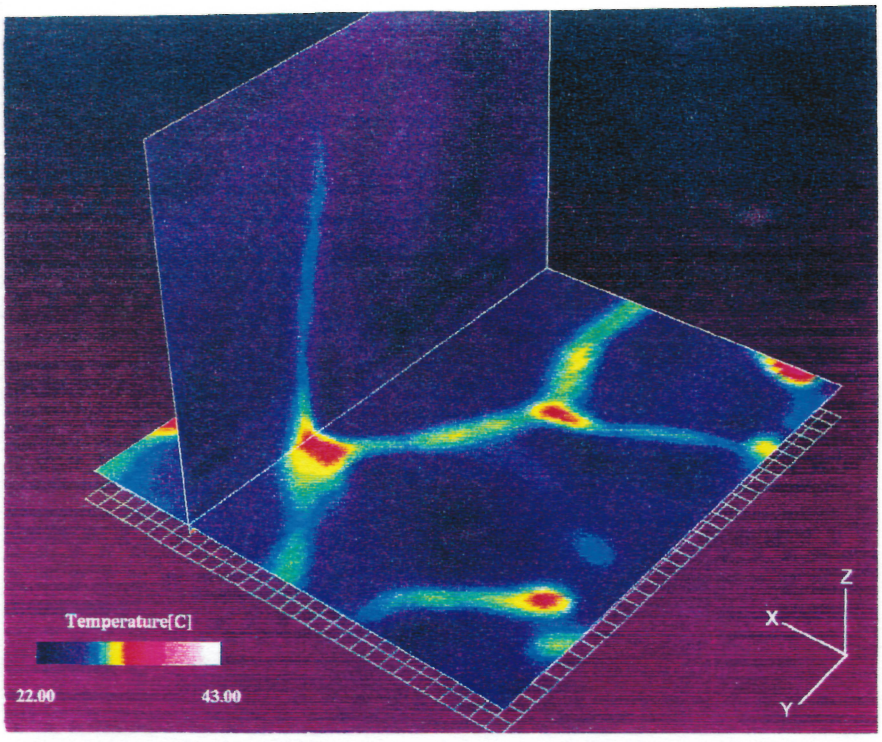

(b) $t = 0.73$ s

Figure 14. Isotherms in a horizontal plane in the vicinity of the heated lower surface.

List of Recent TAM Reports

No.	Authors	Title	Date
779	Phillips, J. W., D. L. de Camara, M. D. Lockwood, and W. C. C. Grebner	Strength of silicone breast implants—*Plastic and Reconstructive Surgery* **97**, 1215–1225 (1996)	Jan. 1995
780	Xin, Y.-B., K. J. Hsia, and D. A. Lange	Quantitative characterization of the fracture surface of silicon single crystals by confocal microscopy—*Journal of the American Ceramics Society* **78**, 3201–3208 (1995)	Jan. 1995
781	Yao, J., and D. S. Stewart	On the dynamics of multi-dimensional detonation—*Journal of Fluid Mechanics* **309**, 225–275 (1996)	Jan. 1995
782	Riahi, D. N., and T. L. Sayre	Effect of rotation on the structure of a convecting mushy layer—*Acta Mechanica* **118**, 109–120 (1996)	Feb. 1995
783	Batchelor, G. K., and TAM faculty and students	A conversation with Professor George K. Batchelor	Feb. 1995
784	Sayre, T. L., and D. N. Riahi	Effect of rotation on flow instabilities during solidification of a binary alloy—*International Journal of Engineering Science* **34**, 1631–1645 (1996)	Feb. 1995
785	Xin, Y.-B., and K. J. Hsia	A technique to generate straight surface cracks for studying the dislocation nucleation condition in brittle materials—*Acta Metallurgica et Materialia* **44**, 845–853 (1996)	Mar. 1995
786	Riahi, D. N.	Finite bandwidth, long wavelength convection with boundary imperfections: Near-resonant wavelength excitation—*International Journal of Mathematics and Mathematical Sciences* **21**, 171–182 (1997)	Mar. 1995
787	Turner, J. A., and R. L. Weaver	Average response of an infinite plate on a random foundation—*Journal of the Acoustical Society of America* **99**, 2167–2175 (1996)	Mar. 1995
788	Weaver, R. L., and D. Sornette	The range of spectral correlations in pseudointegrable systems: GOE statistics in a rectangular membrane with a point scatterer—*Physical Review E* **52**, 341 (1995)	Apr. 1995
789	Students in TAM 293–294	Thirty-second student symposium on engineering mechanics, J. W. Phillips, coordinator: Selected senior projects by K. F. Anderson, M. B. Bishop, B. C. Case, S. R. McFarlin, J. M. Nowakowski, D. W. Peterson, C. V. Robertson, and C. E. Tsoukatos	Apr. 1995
790	Figa, J., and C. J. Lawrence	Linear stability analysis of a gravity-driven Newtonian coating flow on a planar incline	May 1995
791	Figa, J., and C. J. Lawrence	Linear stability analysis of a gravity-driven viscosity-stratified Newtonian coating flow on a planar incline	May 1995
792	Cherukuri, H. P., and T. G. Shawki	On shear band nucleation and the finite propagation speed of thermal disturbances—*International Journal of Solids and Structures*, in press (1996)	May 1995
793	Harris, J. G.	Modeling scanned acoustic imaging of defects at solid interfaces—Chapter in *IMA Workshop on Inverse Problems in Wave Propagation*, eds. G. Chevant, G. Papanicolaou, P. Sacks and W. E. Symes, 237–258, Springer-Verlag, New York (1996)	May 1995
794	Sottos, N. R., J. M. Ockers, and M. J. Swindeman	Thermoelastic properties of plain weave composites for multilayer circuit board applications	May 1995
795	Aref, H., and M. A. Stremler	On the motion of three point vortices in a periodic strip—*Journal of Fluid Mechanics* **314**, 1–25 (1996)	June 1995
796	Barenblatt, G. I., and N. Goldenfeld	Does fully-developed turbulence exist? Reynolds number independence versus asymptotic covariance—*Physics of Fluids* **7**, 3078–3082 (1995)	June 1995
797	Aslam, T. D., J. B. Bdzil, and D. S. Stewart	Level set methods applied to modeling detonation shock dynamics—*Journal of Computational Physics*, **126**, 390–409 (1996)	June 1995

List of Recent TAM Reports (cont'd)

No.	Authors	Title	Date
798	Nimmagadda, P. B. R., and P. Sofronis	The effect of interface slip and diffusion on the creep strength of fiber and particulate composite materials—Proceedings of the ASME Applied Mechanics Division **213**, 125–143 (1995)	July 1995
799	Hsia, K. J., T.-L. Zhang, and D. F. Socie	Effect of crack surface morphology on the fracture behavior under mixed mode loading—*ASTM Special Technical Publication* 1296, in press (1996)	July 1995
800	Adrian, R. J.	Stochastic estimation of the structure of turbulent fields—*Eddy Structure Identification*, ed. J. P. Bonnet, Springer: Berlin 145–196 (1996)	Aug. 1995
801	Riahi, D. N.	Perturbation analysis and modeling for stratified turbulence	Aug. 1995
802	Thoroddsen, S. T.	Conditional sampling of dissipation in high Reynolds number turbulence—*Physics of Fluids* **8**, 1333–1335	Aug. 1995
803	Riahi, D. N.	On the structure of an unsteady convecting mushy layer—*Acta Mechanica*, in press (1996)	Aug. 1995
804	Meleshko, V. V.	Equilibrium of an elastic rectangle: The Mathieu–Inglis–Pickett solution revisited—*Journal of Elasticity* **40**, 207–238 (1995)	Aug. 1995
805	Jonnalagadda, K., G. E. Kline, and N. R. Sottos	Local displacements and load transfer in shape memory alloy composites	Aug. 1995
806	Nimmagadda, P. B. R., and P. Sofronis	On the calculation of the matrix–reinforcement interface diffusion coefficient in composite materials at high temperatures—*Acta Metallurgica et Materialia*, **44**, 2711–2716 (1996)	Aug. 1995
807	Carlson, D. E., and D. A. Tortorelli	On hyperelasticity with internal constraints—*Journal of Elasticity* **42**, 91–98 (1966)	Aug. 1995
808	Sayre, T. L., and D. N. Riahi	Oscillatory instabilities of the liquid and mushy layers during solidification of alloys under rotational constraint—*Acta Mechanica* **121**, 143–152 (1997)	Sept. 1995
809	Xin, Y.-B., and K. J. Hsia	Simulation of the brittle–ductile transition in silicon single crystals using dislocation mechanics	Oct. 1995
810	Ulysse, P., and R. E. Johnson	A plane-strain upper-bound analysis of unsymmetrical single-hole and multi-hole extrusion processes	Oct. 1995
811	Fried, E.	Continua described by a microstructural field—*Zeitschrift für angewandte Mathematik und Physik*, **47**, 168–175 (1996)	Nov. 1995
812	Mittal, R., and S. Balachandar	Autogeneration of three-dimensional vortical structures in the near wake of a circular cylinder	Nov. 1995
813	Segev, R., E. Fried, and G. de Botton	Force theory for multiphase bodies—*Journal of Geometry and Physics*, in press (1996)	Dec. 1995
814	Weaver, R. L.	The effect of an undamped finite-degree-of-freedom "fuzzy" substructure: Numerical solutions and theoretical discussion—*Journal of the Acoustical Society of America* **100**, 3159–3164 (1996)	Jan. 1996
815	Haber, R. B., C. S. Jog, and M. P. Bendsøe	A new approach to variable-topology shape design using a constraint on perimeter—*Structural Optimization* **11**, 1–12 (1996)	Feb. 1996
816	Xu, Z.-Q., and K. J. Hsia	A numerical solution of a surface crack under cyclic hydraulic pressure loading	Mar. 1996
817	Adrian, R. J.	Bibliography of particle velocimetry using imaging methods: 1917–1995—*Produced and distributed in cooperation with TSI, Inc., St. Paul, Minn.*	Mar. 1996
818	Fried, E., and G. Grach	An order-parameter based theory as a regularization of a sharp-interface theory for solid–solid phase transitions—*Archive for Rational Mechanics and Analysis*, in press (1996)	Mar. 1996
819	Vonderwell, M. P., and D. N. Riahi	Resonant instability mode triads in the compressible boundary-layer flow over a swept wing—*International Journal of Engineering Science*, in press (1997)	Mar. 1996
820	Short, M., and D. S. Stewart	Low-frequency two-dimensional linear instability of plane detonation—*Journal of Fluid Mechanics*, in press (1997)	Mar. 1996

List of Recent TAM Reports (cont'd)

No.	Authors	Title	Date
821	Casagranda, A., and P. Sofronis	On the scaling laws for the consolidation of nanocrystalline powder compacts—Proceedings of the IUTAM Symposium on the Mechanics of Granular and Porous Materials (1996)	Apr. 1996
822	Xu, S., and D. S. Stewart	Deflagration-to-detonation transition in porous energetic materials: A comparative model study—*Journal of Fluid Mechanics*, in press (1997)	Apr. 1996
823	Weaver, R. L.	Mean and mean-square responses of a prototypical master/fuzzy structure—*Journal of the Acoustical Society of America*, in press (1996)	Apr. 1996
824	Fried, E.	Correspondence between a phase-field theory and a sharp-interface theory for crystal growth—*Continuum Mechanics and Thermodynamics*, in press (1997)	Apr. 1996
825	Students in TAM 293–294	Thirty-third student symposium on engineering mechanics, J. W. Phillips, coordinator: Selected senior projects by W. J. Fortino II, A. A. Mordock, and M. R. Sawicki	May 1995
826	Riahi, D. N.	Effects of roughness on nonlinear stationary vortices in rotating disk flows—*Mathematical and Computer Modeling*, in press (1996)	June 1996
827	Riahi, D. N.	Nonlinear instabilities of shear flows over rough walls	June 1996
828	Weaver, R. L.	Multiple scattering theory for a plate with sprung masses: Mean and mean-square responses	July 1996
829	Moser, R. D., M. M. Rogers, and D. W. Ewing	Self-similarity of time-evolving plane wakes	July 1996
830	Lufrano, J. M., and P. Sofronis	Enhanced hydrogen concentrations ahead of rounded notches and cracks—Competition between plastic strain and hydrostatic constraint	July 1996
831	Riahi, D. N.	Effects of surface corrugation on primary instability modes in wall-bounded shear flows	Aug. 1996
832	Bechel, V. T., and N. R. Sottos	Measuring debond length in the fiber pushout test—Proceedings of the ASME Mechanics and Materials Conference (1996)	Aug. 1996
833	Riahi, D. N.	Effect of centrifugal and Coriolis forces on chimney convection during alloy solidification—*Journal of Crystal Growth* **179**, 287–296 (1997)	Sept. 1996
834	Cermelli, P., and E. Fried	The influence of inertia on configurational forces in a deformable solid—*Proceedings of the Royal Society of London A*, in press (1996)	Oct. 1996
835	Riahi, D. N.	On the stability of shear flows with combined temporal and spatial imperfections	Oct. 1996
836	Carranza, F. L., B. Fang, and R. B. Haber	An adaptive space–time finite element model for oxidation-driven fracture	Nov. 1996
837	Carranza, F. L., B. Fang, and R. B. Haber	A moving cohesive interface model for fracture in creeping materials	Nov. 1996
838	Balachandar, S., R. Mittal, and F. M. Najjar	Properties of the mean wake recirculation region in two-dimensional bluff body wakes—*Journal of Fluid Mechanics*, in press (1997)	Dec. 1996
839	Ti, B. W., W. D. O'Brien, Jr., and J. G. Harris	Measurements of coupled Rayleigh wave propagation in an elastic plate	Dec. 1996
840	Phillips, W. R. C.	On finite-amplitude rotational waves in viscous shear flows	Jan. 1997
841	Riahi, D. N.	Direct resonance analysis and modeling for a turbulent boundary layer over a corrugated surface—*Acta Mechanica*, in press (1998)	Jan. 1997
842	Liu, Z.-C., R. J. Adrian, C. D. Meinhart, and W. Lai	Structure of a turbulent boundary layer using a stereoscopic, large format video-PIV	Jan. 1997

List of Recent TAM Reports (cont'd)

No.	Authors	Title	Date
843	Fang, B., F. L. Carranza, and R. B. Haber	An adaptive discontinuous Galerkin methods for viscoplastic analysis	Jan. 1997
844	Xu, S., T. D. Aslam, and D. S. Stewart	High-resolution numerical simulation of ideal and non-ideal compressible reacting flows with embedded internal boundaries	Jan. 1997
845	Zhou, J., C. D. Meinhart, S. Balachandar, and R. J. Adrian	Formation of coherent hairpin packets in wall turbulence	Feb. 1997
846	Lufrano, J. M., P. Sofronis, and H. K. Birnbaum	Elastoplastically accommodated hydride formation and embrittlement	Feb. 1997
847	Keane, R. D., N. Fujisawa, and R. J. Adrian	Unsteady non-penetrative thermal convection from non-uniform surfaces	Feb. 1997
848	Aref, H., and M. Brøns	On stagnation points and streamline topology in vortex flows	Mar. 1997
849	Asghar, S., T. Hayat, and J. G. Harris	Diffraction by a slit in an infinite porous barrier	Mar. 1997
850	Shawki, T. G., H. Aref, and J. W. Phillips	Mechanics on the Web—Proceedings of the International Conference on Engineering Education (Aug. 1997, Chicago)	Apr. 1997
851	Stewart, D. S., and J. Yao	The normal detonation shock velocity–curvature relationship for materials with non-ideal equation of state and multiple turning points	Apr. 1997
852	Fried, E., A. Q. Shen, and S. T. Thoroddsen	Traveling waves, standing waves, and cellular patterns in a steadily forced granular medium	Apr. 1997
853	Boyland, P. L., H. Aref, and M. A. Stremler	Topological fluid mechanics of stirring	Apr. 1997
854	Parker, S. J., and S. Balachandar	Viscous and inviscid instabilities of flow along a streamwise corner	May 1997
855	Soloff, S. M., R. J. Adrian, and Z.-C. Liu	Distortion compensation for generalized stereoscopic particle image velocimetry	May 1997
856	Zhou, Z., R. J. Adrian, S. Balachandar, and T. M. Kendall	Mechanisms for generating coherent packets of hairpin vortices in near-wall turbulence	June 1997
857	Neishtadt, A. I., D. L. Vainshtein, and A. A. Vasiliev	Chaotic advection in a cubic Stokes flow	June 1997
858	Weaver, R. L.	Ultrasonics in an aluminum foam	July 1997
859	Riahi, D. N.	High gravity convection in a mushy layer during alloy solidification	July 1997
860	Najjar, F. M., and S. Balachandar	Low-frequency unsteadiness in the wake of a normal flat plate	Aug. 1997
861	Short, M.	A parabolic linear evolution equation for cellular detonation instability	Aug. 1997
862	Short, M., and D. S. Stewart	Cellular detonation stability—I: A normal-mode linear analysis	Sept. 1997
863	Carranza, F. L., and R. B. Haber	A numerical study of intergranular fracture and oxygen embrittlement in an elastic–viscoplastic solid	Oct. 1997
864	Sakakibara, J., and R. J. Adrian	Whole-field measurement of temperature in water using two-color laser-induced fluorescence	Oct. 1997
865	Riahi, D. N.	Effect of surface corrugation on convection in a three-dimensional finite box of fluid-saturated porous material	Oct. 1997